Oscillatory cellular patterns in three-dimensional directional solidification

D. Tourret, J.-M. Debierre, Y. Song, Fatima L. Mota, N. Bergeon, R. Guerin, R. Trivedi, B. Billia, A. Karma

PHYSICAL REVIEW E **92**, 042401 (2015)

Oscillatory cellular patterns in three-dimensional directional solidification

D. Tourret,[1,*] J.-M. Debierre,[2] Y. Song,[1] F. L. Mota,[2] N. Bergeon,[2] R. Guérin,[2] R. Trivedi,[3] B. Billia,[2] and A. Karma[1]

[1]*Department of Physics and Center for Interdisciplinary Research on Complex Systems, Northeastern University, Boston, Massachusetts 02115, USA*

[2]*Institut Matériaux Microélectronique Nanosciences de Provence, Aix-Marseille Université and CNRS UMR 7334, Campus Saint-Jérôme, Case 142, 13397 Marseille Cedex 20, France*

[3]*Department of Materials Science and Engineering, Iowa State University, Ames, Iowa 50010, USA*

(Received 2 June 2015; published 7 October 2015)

We present a phase-field study of oscillatory breathing modes observed during the solidification of three-dimensional cellular arrays in microgravity. Directional solidification experiments conducted onboard the International Space Station have allowed us to observe spatially extended homogeneous arrays of cells and dendrites while minimizing the amount of gravity-induced convection in the liquid. *In situ* observations of transparent alloys have revealed the existence, over a narrow range of control parameters, of oscillations in cellular arrays with a period ranging from about 25 to 125 min. Cellular patterns are spatially disordered, and the oscillations of individual cells are spatiotemporally uncorrelated at long distance. However, in regions displaying short-range spatial ordering, groups of cells can synchronize into oscillatory breathing modes. Quantitative phase-field simulations show that the oscillatory behavior of cells in this regime is linked to a stability limit of the spacing in hexagonal cellular array structures. For relatively high cellular front undercooling (i.e., low growth velocity or high thermal gradient), a gap appears in the otherwise continuous range of stable array spacings. Close to this gap, a sustained oscillatory regime appears with a period that compares quantitatively well with experiment. For control parameters where this gap exists, oscillations typically occur for spacings at the edge of the gap. However, after a change of growth conditions, oscillations can also occur for nearby values of control parameters where this gap just closes and a continuous range of spacings exists. In addition, sustained oscillations at to the opening of this stable gap exhibit a slow periodic modulation of the phase-shift among cells with a slower period of several hours. While long-range coherence of breathing modes can be achieved in simulations for a perfect spatial arrangement of cells as initial condition, global disorder is observed in both three-dimensional experiments and simulations from realistic noisy initial conditions. In the latter case, erratic tip-splitting events promoted by large-amplitude oscillations contribute to maintaining the long-range array disorder, unlike in thin-sample experiments where long-range coherence of oscillations is experimentally observable.

DOI: 10.1103/PhysRevE.92.042401 PACS number(s): 68.08.−p, 64.70.D−, 81.30.Fb, 05.70.Ln

I. INTRODUCTION

Directional solidification is a generic technique for a broad range of situations ranging from metal casting [1–4] to model experiments on interface pattern selection and dynamics [5,6].

Laboratory experiments are usually conducted in a furnace with a hot thermal contact at one end of the container (for instance, the top end) and a cold contact at the other end (the bottom one). Most furnaces are designed to produce a constant temperature gradient G in the material solidifying inside the container. The sample is pulled at constant velocity V toward the cold region, hence imposing solidification at a given rate. For a binary alloy of nominal solute concentration c_∞, the exploration of control parameters V, G, and c_∞ leads to a wide range of structures that adopt a number of forms and dynamics. For V lower than a critical velocity V_c, the solid-liquid interface remains planar, the limit value V_c being known as the Mullins-Sekerka morphological instability threshold [7]. As V is increased beyond V_c, the planar front becomes unstable, and the solidifying material forms fingerlike structures called cells, with a spacing Λ ranging typically from tens to hundreds of micrometers between two cell tips. Dendritic structures with secondary and ternary side arms appear at higher velocities. To date, those interface patterns have been primarily visualized in thin-sample directional solidification experiments using transparent organic alloys, which only allow typically one row of cells or dendrites to form inside the sample (see, e.g., Refs. [8–17]).

During solidification of three-dimensional bulk samples on Earth, thermal and/or solutal gradients combined with gravity usually lead to fluid flow in the liquid [18,19]. The direct consequence of these convective currents is the heterogeneity of microstructures from the core to the side of three-dimensional samples [18]. This is why most observations of solidification microstructure selection and dynamics have historically been restricted to thin-sample experiments, where the size of the sample limits the amount of convection. In the close neighborhood of the critical velocity, typically for $V_c < V < V_c/k$, where $k < 1$ is the interface solute partition coefficient, the cellular regime usually yields a wide variety of structures and dynamics, such as symmetric cells, asymmetric cells, multiplets, as well as a very active elimination and creation of cells.

Among those multiple regimes, breathing modes, which constitute a generic secondary oscillatory instabilities of

*Current address: Los Alamos National Laboratory, Materials Science and Technology Division, Los Alamos, NM 87545, USA; dtourret@lanl.gov.

spatially modulated interface patterns [20], have been reported, such as the 2λ-O mode in which an ordered rank of cells oscillate with a regular π phase shift between two successive cells [13]. Breathing modes have been experimentally and theoretically studied in two dimensions (2D) for both cellular [13,21–23] and two-phase eutectic [24,25] interfaces. In three dimensions, other oscillatory breathing modes have been predicted with three sublattices of a hexagonal array beating with a $\pm 2\pi/3$ phase shift with each other in the high-velocity limit [26] as well as with a two-sided phase-field model [27]. All these oscillatory modes, both theoretically predicted and experimentally observed, exhibit a long-range coherence of oscillation throughout the entire array. However, due to gravity-induced convection, three-dimensional breathing modes were never directly observed in experiments until recently [28].

Three-dimensional directional solidification experiments within a reduced-gravity environment were recently made possible by the development of the Directional Solidification Insert (DSI) of the Device for the study of Critical Liquids and Crystallization (DECLIC) facility installed onboard in the International Space Station (ISS) [29,30]. Unprecedented observations of a transparent alloy directional solidification experiments in space revealed the occurrence of breathing-mode oscillations in spatially extended cellular arrays [28]. Most cells oscillate with a time period of a few tens of minutes but, due to the strong disorder of the cell array, these oscillations remain mostly uncorrelated, i.e., no long-range phase coherence appears. Locally in time and in space, a few neighboring cells synchronize their dynamics to yield a phase opposition or a $2\pi/3$ phase shift depending on the spatial organization of cells. However, these time and space cooperative events remain rare because of the array topological disorder.

In combination with these experiments, we performed large-scale quantitative phase-field simulations, massively parallelized on graphic processing units (GPU). Our simulations were able to produce comparable breathing modes with a time period τ very close to the one measured in experiments, for instance, at $V = 1\ \mu$m/s [28]. In the current article, we propose a more extended analysis of these oscillatory breathing modes in cellular arrays, based on additional phase-field simulations. We specifically explore the conditions of appearance and the origin of such oscillatory modes in three dimensions, the lack (presence) of long- (short-) range spatiotemporal coherence of oscillations, and the dependence of breathing modes and oscillations upon experimental control parameters.

After summarizing our experimental (Sec. II) and numerical (Sec. III) methods, we directly compare the dynamics of spatially extended cellular arrays in experiments and simulations (Sec. IV A). Next, we explain their complex dynamics through calculations of stability conditions for individual cells (Sec. IV B) and simulations of oscillatory regimes under a forced hexagonal symmetry of the cellular array (Sec. IV C). We show the link between oscillatory modes and spacing stability ranges (Secs. IV B and IV D) and the relationship between oscillation coherence and long-range spatial order of the array (Sec. IV C). We then discuss the dependence of oscillations features, i.e., amplitude and period, with experimental control parameters (Secs. IV D and IV E). Finally, conclusions are summarized in Sec. V.

II. DIRECTIONAL SOLIDIFICATION EXPERIMENTS

A. DECLIC-DSI

The experiments in this article were realized within the DSI of the DECLIC developed by the French Space Agency (CNES) and installed onboard the ISS, in the framework of CNES Project MISOL3D (Microstructures de Solidification 3D) and NASA Project Dynamical Selection of 3D Interface Patterns (DSIP). The DECLIC-DSI is dedicated to *in situ* and real-time characterization of solid-liquid interface patterns during directional solidification of transparent alloys. This unique apparatus enables the processing of bulk three-dimensional samples within a negligible gravity environment—approximately 10^{-4} times the Earth's gravity—hence suppressing microstructure inhomogeneities due to convection, unavoidable in bulk experiments on Earth [18].

Since the DECLIC and DSI have already been presented elsewhere [29–31], we focus here on the details pertaining to cellular oscillations. The DECLIC-DSI allows two observation modes of the Bridgman directional solidification experiment, namely along the direction of solidification, z, and from the side of the crucible. The only observation mode discussed here is in the direction of solidification. It is made possible by a flat glass window at the bottom of the crucible and a lens immersed in the liquid at the top. Hence, the light from LEDs at the bottom passes through the solid-liquid interface, reaches the lens in the liquid, and goes through a second relay lens that produces the image of the interface on a charge-coupled-device camera. Therefore, all microstructure images in this article are shown from the liquid side of the interface, with the solid growing toward the observer. Furthermore, on the same observation axis, the setup is equipped with an interferometer, which allows reconstruction of the three-dimensional shape of cells and dendrite tips [30].

B. Directional solidification experiments

A succinonitrile (SCN) (0.24wt%) camphor alloy was prepared from SCN purified by NASA by distillation and zone melting. The sample preparation and cartridge filling were realized under vacuum to avoid humidity contamination. Once sealed, the cartridge was inserted into the Bridgman furnace. The experimental cartridge includes a quartz crucible and a system of volume compensation. The cylindrical crucible has an inner diameter of 10 mm and a length that enables about 10 cm of solidification, thus allowing the study of the interface pattern dynamics from the onset of morphological instability to the microstructural steady state.

The thermal gradient G is imposed by regulating the hot and cold zones temperatures, located above and below the adiabatic zone containing the interface. After thermal regulation, the sample is partially melted, keeping a solid seed to preserve the crystal orientation, and homogenized for 24 h. Solidification proceeds by pulling the crucible into the cold zone at a constant velocity V.

While the DECLIC-DSI enables the study of various complex patterns, from planar to cellular to dendritic, we only

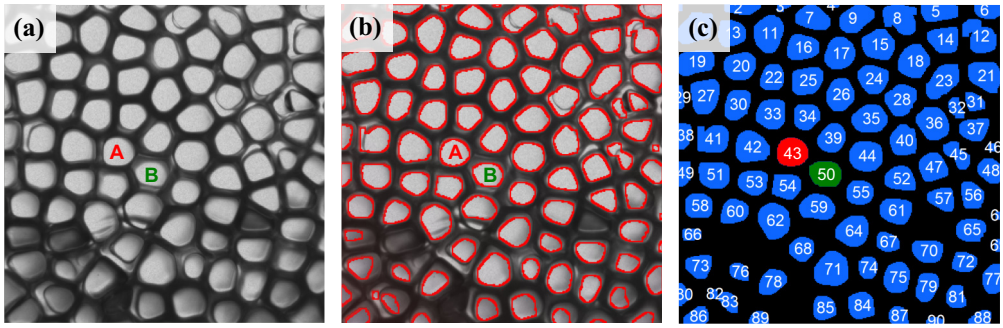

FIG. 1. (Color online) Image processing steps for the experimental videos: (a) Initial raw image (3.2×3.2 mm^2); (b) contours of apparent surface of cell caps on corrected binary image superimposed to the initial image; (c) tagged binary image. Cells A and B correspond to the cells analyzed in Fig. 2. The raw video (a) is provided in the Supplemental Material [32].

focus here on a range of parameters that yields oscillations of a cellular array. These oscillations can be observed both on the vertical position of the cell tip in z and on the cell area seen from the growth direction. Here we base our analysis on the time evolution of the apparent cell area in the direction of solidification, as described in the following subsection.

C. Postprocessing

Details of the image processing of the microgravity experiment already have been published [30]. Measurements of apparent surface $A(t)$ of cell caps seen from the top are done with the software VISILOG using macroprocedures specifically developed for the systematic processing of microgravity experiments images.

Starting with the raw image of the interface [Fig. 1(a)], each initial gray-level image is transformed into a binary image after defining a threshold value that ensures that a large majority of cells are disconnected from their neighbors. Then, in order to get rid of defects originating from tip-splitting events and from brighter regions at groove bottoms, we used the *Opening function* of VISILOG, which removes small objects and defects and hence disconnects particles. The resulting threshold image permits us to identify the apparent contour of cells, as shown in Fig. 1(b), by superimposing the original image with the surfaces contour. One can then tag each cell [Fig. 1(c)] and follow the evolution in time of its position and area. In order to track individual cells in time, we consider that each cell conserves its index if its center in the new image $n+1$ is located within its area on the previous image n. For the present example of images in Fig. 1 at a pulling rate $V = 1$ μm/s, raw images were acquired at a frequency of 0.5 image/s. Yet it was sufficient to analyze a series of images sampling at one image per minute to obtain unbiased measurements and respect the tagging procedure.

Then, using *gnuplot*, we fitted the time evolution of the cell areas $A(t)$ to a periodic function $a + bt + c\sin[2\pi(t-t_0)/\tau]$, where a, b, c, t_0, and τ are free fitting parameters, as illustrated in Fig. 2. The linear baseline of oscillation $a+bt$ was found to provide a better fit to the experimental data (the fit with $b=0$ is not illustrated in Fig. 2). Hence, the sinusoidal fits readily provide the value of the oscillation period τ and the oscillation phase $\theta(t) = 2\pi(t-t_0)/\tau$ for each cell. Note that cells A and B in Figs. 1 and 2, also corresponding to results in Fig. 8(a), exhibit an example of short-range oscillation correlation with two neighbor cells oscillating in phase opposition.

III. PHASE-FIELD SIMULATIONS

A. Phase-field model

The phase-field model used here is based on the thin-interface one-sided model with corrective antitrapping current developed in Refs. [33,34], for the solidification of a dilute binary alloy at an imposed pulling velocity V within a temperature gradient of amplitude G, both in the z direction, such that the temperature profile follows

$$T = T_0 + G(z - Vt), \tag{1}$$

where T_0 is the reference (i.e., solidus) temperature for an alloy of nominal solute concentration c_∞. In order to enhance numerical stability for larger grid spacings [35], the equations of evolution of the phase field φ and the dimensionless solute field U—i.e., Eqs. (68) and (69) in Ref. [33]—are written as a function of the preconditioned phase field ψ with

$$\varphi(x,y,z,t) = \tanh\left\{\frac{\psi(x,y,z,t)}{\sqrt{2}}\right\}. \tag{2}$$

Since the 1D phase-field solidification problem admits an explicit traveling wave solution which has the form $\varphi(z,t) \sim -\tanh[(z-\widetilde{V}t)/\sqrt{2}]$, Eq. (2) makes $\psi(x,y,z,t)$ similar to a signed distance function from a planar interface. In terms of

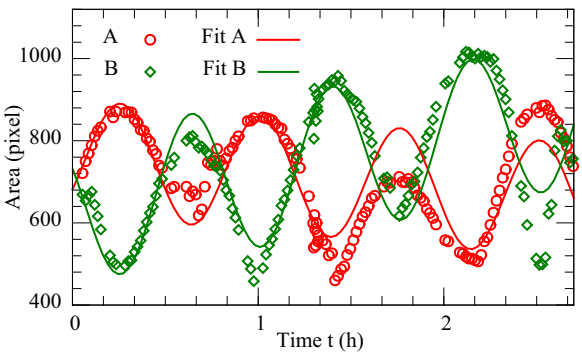

FIG. 2. (Color online) Time evolution of the areas of cells A and B in Fig. 1 (symbols), fitted to sinusoidal functions (lines).

this preconditioned phase field, the equations of the model become

$$\left[1-(1-k)\frac{z-\widetilde{V}\,t}{\widetilde{l}_T}\right]a_s(\mathbf{n})^2\frac{\partial\psi}{\partial t} = \vec{\nabla}[a_s(\mathbf{n})^2]\vec{\nabla}\psi + a_s(\mathbf{n})^2[\nabla^2\psi - \varphi\sqrt{2}|\vec{\nabla}\psi|^2] + \sum_{m=x,y,z}\left\{\partial_m\left[|\vec{\nabla}\psi|^2 a_s(\mathbf{n})\frac{\partial a_s(\mathbf{n})}{\partial(\partial_m\psi)}\right]\right\} + \varphi\sqrt{2} - \lambda(1-\varphi^2)\sqrt{2}\left(U+\frac{z-\widetilde{V}\,t}{\widetilde{l}_T}\right), \quad (3)$$

$$[1+k-(1-k)\varphi]\frac{\partial U}{\partial t} = \widetilde{D}\,\vec{\nabla}\cdot[(1-\varphi)\vec{\nabla}U] + \vec{\nabla}\cdot\left\{[1+(1-k)U]\times\frac{(1-\varphi^2)}{2}\frac{\partial\psi}{\partial t}\frac{\vec{\nabla}\psi}{|\vec{\nabla}\psi|}\right\} + [1+(1-k)U]\frac{(1-\varphi^2)}{\sqrt{2}}\frac{\partial\psi}{\partial t}, \quad (4)$$

where

$$U = \frac{1}{1-k}\left[\frac{c/c_l^0}{(1-\varphi)/2+k(1+\varphi)/2}-1\right] \quad (5)$$

is the dimensionless supersaturation with c the solute concentration, $c_l^0 = c_\infty/k$ is the solute concentration of a flat interface at the solidus temperature T_0, and k is the interface solute partition coefficient. Space is in units of the phase-field diffuse interface width W and time is in units of the relaxation time τ_0 at the temperature T_0 [33]. Thus, the nondimensional values of the diffusion coefficient $\widetilde{D}$, pulling velocity $\widetilde{V}$, and thermal length $\widetilde{l}_T$ are

$$\widetilde{D} = \frac{D\tau_0}{W^2} = a_1 a_2\frac{W}{d_0}, \quad (6)$$

$$\widetilde{V} = \frac{V\tau_0}{W} = a_1 a_2\frac{Vd_0}{D}\left(\frac{W}{d_0}\right)^2, \quad (7)$$

$$\widetilde{l}_T = \frac{l_T}{W} = \frac{l_T}{d_0}\frac{1}{W/d_0}, \quad (8)$$

and the coupling factor

$$\lambda = a_1\frac{W}{d_0}, \quad (9)$$

where D is the solute diffusion coefficient in the liquid, $l_T = mc_\infty(1-1/k)/G$ is the thermal length with m the liquidus slope, and $d_0 = \Gamma/[mc_\infty(1-1/k)]$ is the capillarity length with Γ the Gibbs-Thomson coefficient of the solid-liquid interface, $a_1 = 5\sqrt{2}/8$, and $a_2 = 47/75$ [36,37]. We consider the standard form of the surface tension anisotropy $\gamma(\mathbf{n}) = \bar{\gamma}a_s(\mathbf{n})$ for a cubic material

$$a_s(\mathbf{n}) = (1-3\epsilon_4)\left[1+\frac{4\epsilon_4}{1-3\epsilon_4}\left(n_x^4+n_y^4+n_z^4\right)\right], \quad (10)$$

where $\bar{\gamma}$ is the average surface tension in a $\langle 100\rangle$ plane, $\mathbf{n}$ is the unit normal vector to the interface pointing toward the liquid phase, and ϵ_4 is the anisotropy strength. In our simulations, the crystallographic axes are aligned with the coordinate system. Since the interface normal $\mathbf{n} = -\vec{\nabla}\psi/|\vec{\nabla}\psi|$ can identically be substituted by $\mathbf{n} = -\vec{\nabla}\varphi/|\vec{\nabla}\varphi|$, we use the latter because the steeper variation of φ through the interface yields a more accurate direction of the normal $\mathbf{n}$. Also, note that the notation φ in Eqs. (3) and (4) only stands for $\tanh(\psi/\sqrt{2})$.

B. Implementation

The phase-field Eqs. (3) and (4) are solved on a grid of cubic elements of dimension Δx using finite differences and a Euler explicit time-stepping scheme with a time step Δt. The expressions of the second and third terms in the right-hand side of Eq. (3) are fully developed, while the first and second terms in the right-hand side of Eq. (4) are discretized in a similar fashion as described in the Appendix B of Ref. [33]. Further details on the implementation of the corresponding 2D model can be found in Ref. [38].

The model is implemented for massively parallel computation on a GPU with the CUDA programming language [39]. The implementation does not make advanced use of the GPU shared memory, which means that the cache memory is handled by the GPU itself. The time loop is thus composed of two main kernel calls, one for the calculation of ψ at the next time step and one for the calculation of U at the next time step; the time stepping is then achieved by swapping pointer addresses between arrays containing values of ψ and U at the current time step and arrays containing values at the next time step. We apply a periodical shift of the domain in the z direction in order to follow the solid-liquid interface.

Additionally, we may choose to add a small random noise to represent microscopic fluctuations at the origin of the initial planar interface destabilization. This is achieved by adding a term $\delta_{i,j,k}F_\psi\sqrt{\Delta t}$ to the value of ψ at the next time step, where $\delta_{i,j,k}$ is a random number generated with a flat distribution in the range $[-0.5,0.5]$ for each grid point (i,j,k). While a more quantitative incorporation of noise in the diffusion field is possible [34,40], the present formulation introduces small fluctuations in the system minimizing the computational cost of noise addition. The amplitude of the noise F_ψ was taken here equal to 0.01 or 0.02 (see Sec. III D), which corresponds to the order of magnitude obtained from a quantitative analysis [40,41].

C. Parameters

Nominal parameters for the SCN-camphor alloy, which can be found in the literature [42,43], are summarized in Table I. For different pulling velocities, namely $V = 0.75$, 1.0, 1.5, and 2.0 μm/s, simulations are respectively achieved with a diffuse interface width $W/d_0 = 95$, 79, 63, and 67, and a finite difference grid spacing $\Delta x/W = 1.2$, 1.2, 1.2, and 1.0, such that $\Delta x \sim V^{-1/2}$ with, respectively, $\Delta x \approx 6.0$, 5.0, 4.0 and 3.5 μm. The time step is always taken as $\Delta t \approx \Delta x^2/(6D)$.

While most simulations in this article are achieved with a value of interface anisotropy $\epsilon_4 = 0.007$, some simulations also use a slightly higher crystalline anisotropy $\epsilon_4 = 0.011$. This value of ϵ_4 was suggested by recent experimental measurements of cell and dendrite tip shapes in SCN alloy, which

TABLE I. Physical parameters of the dilute succinonitrile-camphor alloy.

Parameter	Symbol	Value	Unit
Camphor concentration	c_∞	0.24	wt%
Liquid diffusion coefficient	D	270	μm^2/s
Solute partition coefficient	k	0.21	
Liquidus slope	m	−1.365	K/wt%
Gibbs-Thomson coefficient	Γ	0.0648	Kμm
Anisotropy strength	ϵ_4	0.007	

yielded a higher value than initially estimated [44]. When using $\epsilon_4 = 0.011$, simulations at various pulling velocities $V = 0.5$, 0.75, 1.0, 1.1, 1.2, and 1.5 μm/s, respectively, use $W/d_0 = 95$, 95, 79, 63, 63, and 63, together with $\Delta x/W = 1.2$ for all velocities.

The value of the thermal gradient at the interface is not directly measured in the DECLIC-DSI. A value of $G = 28$ K/cm was originally estimated from the change of interface position at rest under a change of temperature of the hot and cold temperature-controlled zones. However, a lower value of $G = 19$ K/cm was recently estimated from additional heat transfer calculations as well as theoretical modeling of planar interface recoil measurements prior to interface destabilization [31]. The latter study, together with additional simulations to be presented elsewhere, indicate that interface recoil measurements can be quantitatively fitted with different thermal drift parameters for values of G ranging approximately between $G = 12$ and $G = 19$ K/cm. Hence, we have chosen to investigate oscillatory modes for a range of values of G guided by those estimates. The present simulations show that a value of G in the lower range of those estimates yields a better agreement with experimentally observed spacings. Simulations for larger values of G up to the initial upper bound of 28 K/cm also provide broader insights into the effect of the temperature gradient and are thus presented in this article.

A recent study on the initial transient recoil of the planar interface [31] has also highlighted uncertainties on the partition coefficient k that could have a value as low as 0.138 in the considered composition range. As previously discussed in Ref. [28] (discussion pertaining to Fig. 3) as well as in Sec. IV E of the present article, the initially considered parameters $G = 28$ K/cm and $k = 0.21$ tend to overestimate the critical velocity $V_c = DGk/[(k-1)mc_\infty] \approx 0.61$ μm/s, while a cellular pattern is already apparent for $V = 0.5$ μm/s in the experiments. Both a lower temperature gradient and a lower partition coefficient could be at the origin of this discrepancy. In this article, we chose to keep the value $k = 0.21$ found in the literature [42,43] and explore only the influence of control parameters G and V.

While the thermal configuration in the experimental setup, and the subsequent thermal history during the experiment, is more complex than initially anticipated [31], the objective of the present article is not to investigate the thermal evolution of the experimental setup. Hence, we only use the comparison between frozen temperature profiles for a temperature gradient from $G = 28$ K/cm to $G = 12$ K/cm to discuss thermal effects on the oscillatory dynamics of cellular patterns. Other

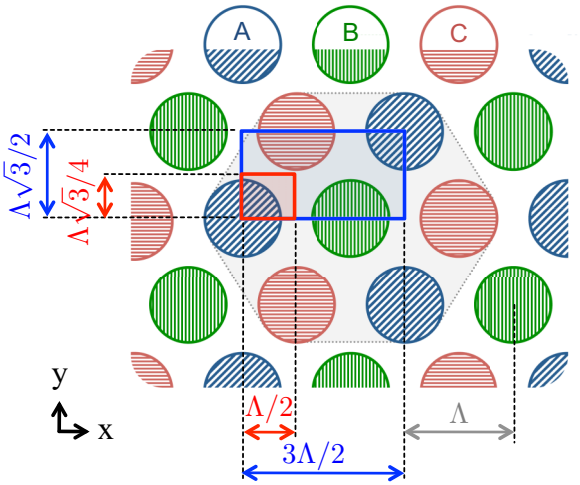

FIG. 3. (Color online) Schematics of the domains for the simulation of hexagonal arrays of cells. A quarter of cell in such an array of spacing Λ can be obtained by simulating a domain of size $\Lambda/2 \times \Lambda\sqrt{3}/4$ in $x \times y$ (red box) with no-flux boundary conditions in x and at the low y boundary and an "antisymmetric" boundary condition on the top y boundary (see text). A hexagonal array of cells containing three groups of cells A, B, and C can be simulated with 1.5 cells within a domain of size $3\Lambda/2 \times \Lambda\sqrt{3}/2$ in $x \times y$ (blue box) with no-flux boundary conditions in y and "helical" boundary conditions on x (see text).

effects that have not so far been accounted for in simulations but have been evidenced in experiments include the effect of the interface curvature on microstructure selection, and the influence of the homogenization time (24 h in the present experiments), which is associated with the establishment of a solute boundary layer in the liquid that may affect the dynamical selection of microstructures [45].

D. Simulations

1. *Spatially extended simulation*

The spatially extended simulation presented in Sec. IV A starts with a planar interface at rest at the liquidus temperature, with homogeneous concentration in the bulk liquid and solid (at $\varphi \approx \pm 1.0$). Thus, we set $\psi(x,y,z,t=0) = z - \tilde{l}_T$, since ψ is a signed distance function with $z = 0$ at the solidus temperature, and $U(x,y,z,t=0) = -1.0$ throughout the entire domain. The total size of the simulation domain is $1005 \times 1005 \times 4061$ μm^3, i.e., $152 \times 152 \times 608$ grid points in x, y, and z respectively, simulated over 10 h of experiment, with no-flux boundary conditions on the boundaries normal to the growth direction z and periodic boundary conditions on the boundaries normal to x and y. We destabilize the planar interface by enabling noise with $F_\psi = 0.01$ in the equation of motion of ψ. The simulation was achieved in less than 67 h on a single GPU.

2. *Identification of spacings stability ranges*

The second series of simulations consists in identifying the spacing stability range of a single cell in a hexagonal array. To do so, we simulate one quarter of a cell in a hexagonal array. We enforce hexagonal symmetry by using boundary conditions

illustrated in Fig. 3 (red domain) and a dimension ratio L_Y/L_X as close as possible to $\sqrt{3}/2$ using an integer number of grid points. The boundary conditions on the x boundaries as well as on the lower y boundary are no-flux, while the conditions at the higher y boundary are "antisymmetric." This latter condition is similar to a no-flux condition with an additional reflexion with respect to x, i.e., the boundary condition on a field $f(x,y,z)$ is $f_{i,N_y,k} = f_{N_x+1-i,N_y-1,k}$, where (i,j,k) are grid indices corresponding the (x,y,z) coordinates; (N_x,N_y,N_z) are the number of grid points in (x,y,z), i.e., $1 \leqslant i \leqslant N_x$, $1 \leqslant j \leqslant N_y$, and $1 \leqslant k \leqslant N_z$; and the boundary condition is applied on the plane defined by $j = N_y - 1/2$.

First, starting with the initial condition of a planar interface at rest at the liquidus temperature, we simulate a small spacing $\Lambda \approx 50$ μm for different temperature gradient G and velocities V. We activate the destabilization of the system by enabling noise with $F_\psi = 0.01$ in the equation of evolution of ψ. Then we use the final states obtained in these simulations as the initial condition for ψ and U in simulations at progressively larger spacings Λ, i.e., with a greater number of grid points in x and y, by stretching and bilinearly interpolating values of ψ and U. We repeat that procedure until we reach the end of the stable branch in Λ, usually occurring with a tip splitting of the cell.

Typically, we represent a stable state by plotting the cell tip undercooling as a function of the cell spacing (as in Fig. 10), where the cell tip undercooling is calculated from the position of the tip z_{tip} as $\Delta = 1 - z_{\text{tip}}/\tilde{l}_T$. It is worth mentioning that since we did not investigate here the lower limit of spacing, some states reported in Fig. 10 at low Λ may be metastable with respect to cell elimination [34].

In some cases, a gap appears in the spacing stability range (see Sec. IV B), with a second branch of stable states at larger spacings. In order to find this second branch, we start from a lower temperature gradient that does not exhibit a gap in the stable spacing range and impose a temperature gradient ramp with time to reach the investigated gradient. We repeat that procedure for progressively higher gradients until we find no more stable state. [For instance, in Fig. 10(a) discussed later, the rightmost stable branch of solutions is obtained by starting from a stable structure on the continuous branch at $G = 12$ K/cm, and then progressively increasing G until the high-Λ branch disappears.]

Each simulation, corresponding to each individual point in Fig. 10, typically lasted between 45 s and 45 min on a single GPU. For instance, simulations in Fig. 10(a) at $V = 1$ μm/s and $G = 10$ K/cm over 2 h were achieved in 45 s (for $\Lambda \approx 54$ μm) to 41 min (for $\Lambda \approx 483$ μm).

3. *Hexagonal array simulations*

In the final series of simulations, we study the coherent oscillations of three groups of cells in a hexagonal array. To do so, we use the quarter of cell obtained from the simulations described above and repeat it symmetrically 6 times as shown in Fig. 3 (blue domain) with no-flux boundary conditions in y and "helical" boundary conditions in x. This latter condition is equivalent to a periodic boundary condition with an additional reflexion with respect to y, i.e., $f_{1,j,k} = f_{N_x-1,N_y+1-j,k}$ and $f_{N_x,j,k} = f_{2,N_y+1-j,k}$ if the boundary condition is applied to $f(x,y,z)$ on the planes $i = 3/2$ and $i = N_x - 1/2$. Noise in these simulations is with $F_\psi = 0.02$.

The typical simulation time for such simulation on a single GPU is between 5 and 25 h. For instance, the simulation of Fig. 12(b) at $G = 28$ K/cm and $V = 1$ μm/s over 20 h lasted 7 h, and the simulation of Fig. 13 at $G = 13$ K/cm and $V = 1$ μm/s over 50 h lasted 25 h.

E. Postprocessing

We process the images of the solid-liquid interface, i.e., the contour $\psi(x,y,z) = 0$, using the software tools PARAVIEW and IMAGEJ. In Fig. 4, the outer square shows the simulation domain of cross section 1005×1005 μm^2 in $x \times y$, with periodic boundary conditions, seen from the liquid side, like in the experimental pictures. The raw image of the solid-liquid interface appears in Fig. 4(a). We calculate the intersect of the interface $\psi(x,y,z) = 0$ with an isothermal plane $z = z_0$ located between the z locations of the tips and that of the grooves between cells. From this intersection, plotted in blue in Fig. 4(b), we build a binary image of the areas, as shown in Fig. 4(c) (colors and annotations were only added to the black-and-white image for the sake of the discussion in the following paragraphs). Next, we process the sequence of binary images of cells in order to number the cells, get the location of their centers, and calculate their areas. This processing step is performed using a specifically designed script within IMAGEJ. Each cell is followed in time using a

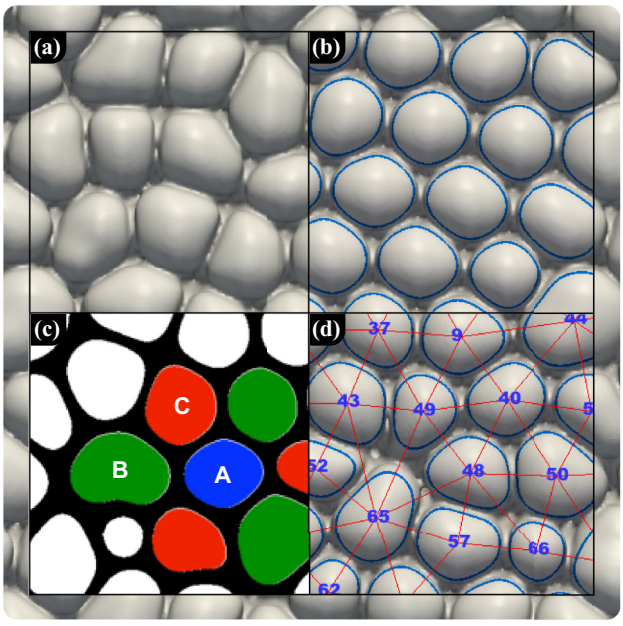

FIG. 4. (Color online) Postprocessing steps of the phase-field simulations: (a) Solid-liquid interface, i.e., contour $\psi(x,y,z) = 0$ seen from the liquid; (b) isothermal intersect (blue lines) of the interface; (c) binary image of the areas of cells; and (d) final processed result with numbered cells and Delaunay triangulation from the centers of cells. The three cells labeled A, B, and C in (c) correspond to the cells illustrated in Figs. 5 and 8(b). Movies of the entire simulation represented as in (a) and (d) are presented in the Supplemental Material [32].

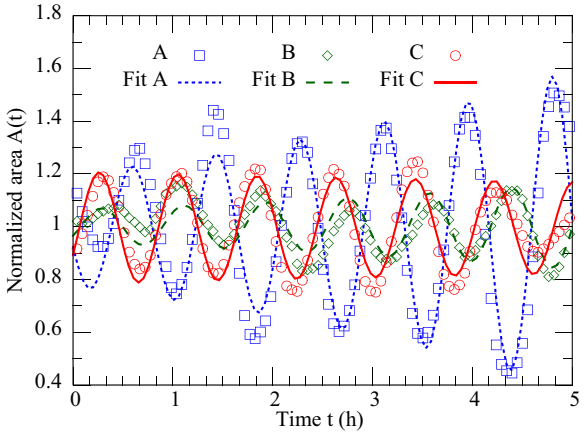

FIG. 5. (Color online) Time evolution of the areas of cells A, B, and C of Fig. 4(c). The areas of cells (symbols) are fitted to a sinusoidal function (lines) in order to extract their oscillation period τ.

criterion of proximity of cell centers from frame to frame. New cells originating from tip-splitting events are attributed a free index, while eliminated cells leave an index vacant. Additionally, that script builds a Delaunay triangulation with the location of the center of the cells and produces the final result illustrated in Fig. 4(d). The videos of the interface before [Fig. 4(a)] and after [Fig. 4(d)] such postprocessing are presented in the Supplemental Material [32].

We process each frame of the movie with this procedure in order to obtain the time evolution of the projected area of each cell. Symbols in Fig. 5 show the areas $A(t)$ of cells A, B, and C from Fig. 4(c), each of them normalized by its average value in time. Then the values of $A(t)$ are fitted to a periodic function $a + b\exp(c\,t)\,\sin[2\pi(t - t_0)/\tau]$ using the software *gnuplot*, where a, b, c, t_0, and τ are free fitting parameters. The fitted functions for cells A, B, and C appear as lines in Fig. 5. The exponential part of the fitting function was introduced to facilitate fitting when the oscillation amplitude is increasing or decreasing, e.g., for Cell A in Fig. 5.

Finally, we extract the oscillation phase of each cell by plotting $A(t + \tau/4)$ vs $A(t)$, such as in Fig. 6(a), where the

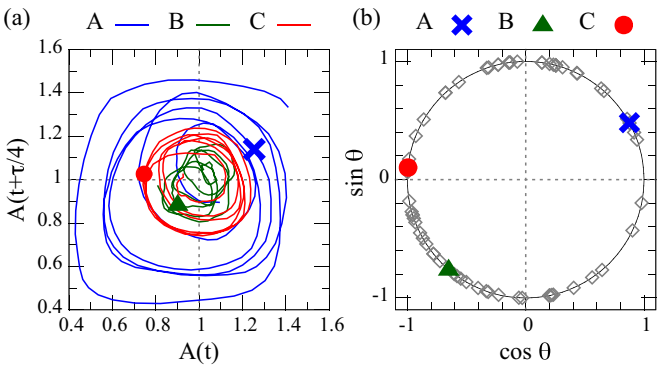

FIG. 6. (Color online) Trajectories of the normalized areas of cells A, B, and C of Fig. 4 in the $[A(t), A(t + \tau/4)]$ plane (a) and phases of all cells at a given time t on the unit circle (b), where cells A, B, and C appear as larger full symbols.

trajectories of cells A, B, and C appear oscillating around their time average (1,1). Hence, at a given time t, for which cells A, B, and C are marked as symbols in Fig. 6(a), the oscillation phase of each cell is directly obtained as $\theta(t) = \arctan\{[A(t + \tau/4) - 1]/[A(t) - 1]\}$. The phases of all cells in the simulation of Fig. 4 at a given time t are reported on the unit circle in Fig. 6(b), where cells A, B, and C are marked with larger symbols.

IV. RESULTS AND DISCUSSION

A. Spatially extended cellular arrays

Experimental *in situ* observations reveal that, for a range of velocities yielding cellular interface patterns, the whole 3D array may exhibit an oscillatory behavior. For an estimated experimental temperature gradient $G \approx 19$ K/cm, oscillations appear from $V = 0.5$ to 1.5 μm/s. Oscillations affect small regions of the cell array when $V = 0.5$ μm/s, the whole pattern oscillates for $V = 1.0$ μm/s, and oscillations are only transient for $V = 1.5$ μm/s. We illustrate this oscillatory behavior for $V = 1$ μm/s in Fig. 7, with an experimental picture in Fig. 7(a) and a phase-field simulation at $G = 28$ K/cm in Fig. 7(b).

This oscillatory behavior is characterized by an oscillation in time of the apparent area $A(t)$ of each cell, together with the oscillation of the cell tip height in z obtained from interferometry [46]. The amplitude of $A(t)$ oscillations may either stay constant or increase, in which case cells eventually split into two cells, and then one of these two cells usually oversteps and eliminates the other as oscillation resumes. This behavior represents a major difference with that reported so far in thin-sample experiments. Indeed, in confined thin-sample experiments, cell tip splitting usually inhibits oscillations by stabilizing the local interface as a multiplet structure [13].

Typically, as illustrated in Fig. 7(a), experiments show a complex interface dynamics, with a constantly evolving spatial organization of cells, nourished by regular tip-splitting events. At the onset of planar destabilization, the cellular array is very disordered, and it then evolves towards a relatively more spatially ordered pattern. However, the resulting pattern is still rather irregular, as can be seen from the cells tagged with their number of immediate neighbors on the right side of Fig. 7 (a perfect hexagonal pattern should lead to a uniform distribution of cells tagged with the number 6), as well as from the ring-shaped appearance of the fast Fourier transform of the experimental pattern ["FFT" inset in Fig. 7(a)]. While tip-splitting events are not at the origin of the initial array disorder, their frequent occurrences have a critical influence in maintaining a significant amount of spatial disorder in the array. Tip-splitting events are often observed to occur at the late stage of a growing oscillation, when the cell area exceeds a threshold favoring the division of one cell into two cells. Even though the pattern does not display any long-range order, it often exhibits local short-range order, in the form of regions with square or hexagonal spatial arrangement of cells, labeled *Hexagon* and *Square* in Fig. 7.

This oscillatory behavior, and its features—namely the lack of long-range spatial order, maintained by the occurrence of tip-splitting events, and the existence of locally ordered

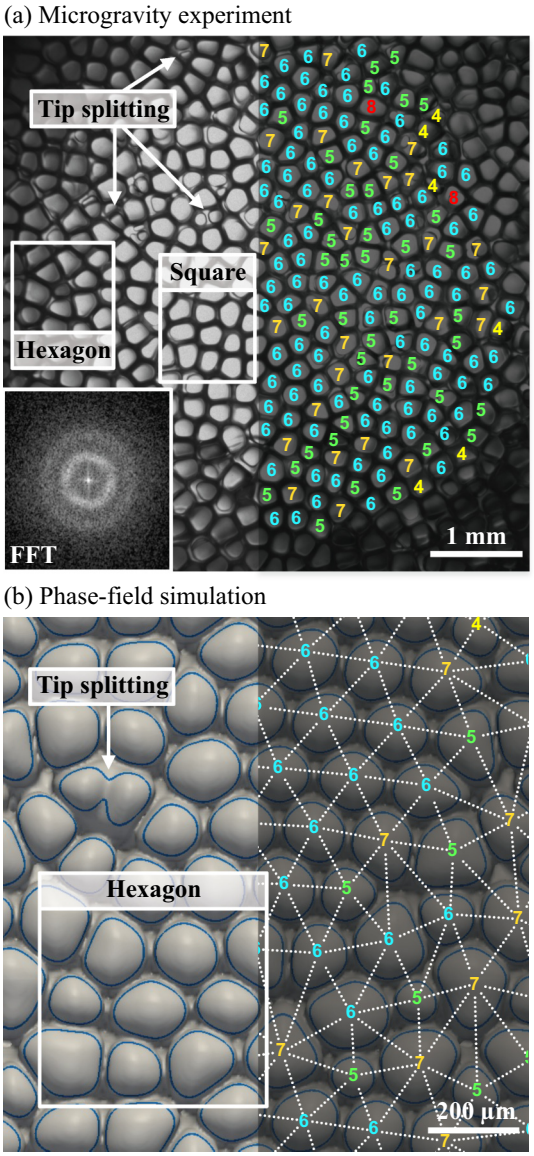

FIG. 7. (Color online) Oscillating cellular pattern observed from the liquid side at $V = 1\ \mu$m/s in the experiment at $G \approx 19$ K/cm (a) and in the phase-field simulation at $G = 28$ K/cm (b). The high spatial disorder of the array is highlighted by both the ring-shaped fast Fourier transform of the image ["FFT" inset in (a)] and the large number of array defects (the number of nearest neighbors of each cell is indicated on the right-hand side). Tip-splitting events are at the origin of the creation and subsequent elimination of new cells in the array, hence preventing the array from stabilizing as a perfect hexagonal arrangement. All cells oscillate with nearly the same period but different phases. However, as illustrated in Fig. 8, in locally ordered regions, regular hexagonal or square patterns exhibit coherent breathing-mode oscillations.

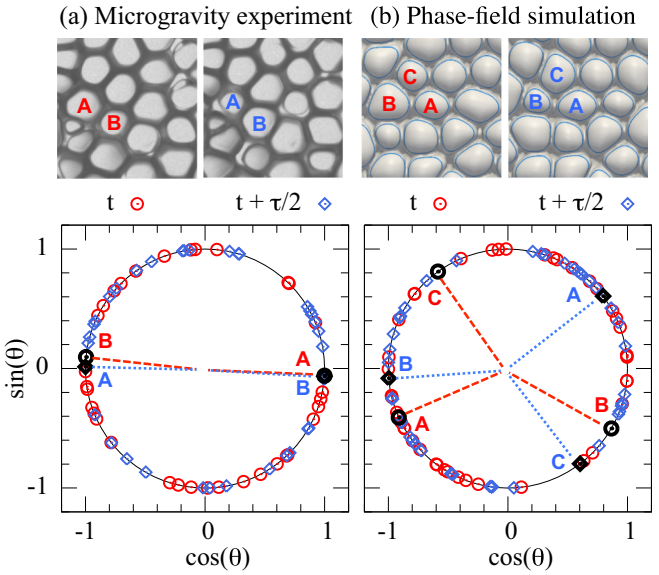

FIG. 8. (Color online) Oscillation phases θ plotted on the unit circle at 2 times half a period ($\tau/2$) apart with different colors and symbols for the experiment (a) and the simulation (b) from Fig. 7. The large scatter of phases indicates the absence of global coherence of oscillations. However, in locally ordered regions, temporary synchronization between first-neighbor cells appears in both experiment and simulation, either with phase opposition (a) or with a $\pm 2\pi/3$ phase shift (b), which correspond to the basic breathing modes.

regions—are reproduced by the phase-field simulation in Fig. 7(b). Like in the experiments, oscillations commonly lead to tip splitting when their amplitude exceeds a threshold. Similarly as in experiments, every cell in the array oscillates with an oscillation period that is insensitive to the spatial order and is remarkably homogeneous throughout the array, with a range of frequencies from the fit of a periodic function (see Sec. III E) from $\tau = 42.7$ to 52.7 min, in good agreement with the average experimental period $\tau = 45.6$ min at $V = 1\ \mu$m/s.

While the oscillation period is uniform throughout array, cells do not display a long-range coherence of oscillations. This is illustrated in Fig. 8, where we plot the oscillation phase of all cells on the unit circle at 2 times half a period apart, in the experiment [Fig. 8(a)] and the phase-field simulation [Fig. 8(b)]. The distribution of phases on the unit circle shown in Fig. 8 reveals a large scatter of phases, therefore highlighting the absence of global coherence, unlike in thin-sample experiments [13]. However, in regions where some spatial order is maintained long enough, a synchronization of oscillations among neighbor cells appears. This is shown in Fig. 8 for two neighbor cells A an B in the experiment, which are beating in opposition of phase, i.e., with a π phase difference, as well as for three cells A, B, and C within a hexagonal arrangement in the phase-field simulation, beating with a phase difference of approximately $2\pi/3$. The phase differences in Fig. 8(b) are not exactly $2\pi/3$, as the phase difference between A and C seems closer to $\pi/2$ with the two complementary phase differences around $3\pi/4$. That deviation from a perfect $2\pi/3$ breathing-mode oscillation is discussed in Sec. IV C and explained by the presence of a second oscillatory behavior, with phase differences oscillating around $2\pi/3$ with a longer oscillation period.

While the breathing modes illustrated in Fig. 8 lead to a short-range phase coherence, this synchronization does not extend beyond immediately neighboring cells, in contrast

to previous thin-sample experiments [13]. As discussed throughout this section, the oscillatory behavior of individual cells are independent of the array topology. However, their synchronization into a $2\pi/3$ breathing mode strongly depends on the (local) hexagonal symmetry of the cellular array. Hence, in our experiments, defects such as the common penta-hepta defect tend to prevent the synchronization of cells into a $2\pi/3$ breathing mode. The lack of long-range oscillations coherence thus appears to be linked to the high disorder within the array, as discussed in Sec. IV C.

Both our experiment and simulation exhibit mostly penta-hepta defects, appearing as five-seven pairs on the right-hand side of Fig. 7. These penta-hepta defects are the most generic type of defects in hexagonal patterns and they have been thoroughly studied theoretically (see, e.g., Refs. [47,48]). Defects in general are known to play a key role in the process of pattern selection, and hexagonal patterns are among the most common in spatially extended nonequilibrium systems [49], observed in a broad range of experiments such as in non-Boussinesq Rayleigh-Bénard convection [50], Bénard-Marangoni convection [51], Turing structures in chemical reactions [52], soap bubbles [53], and nonlinear optics [54], to name only a few.

The amount of defects in Fig. 7 is too high to make conclusive observations on the dynamics and trajectory of isolated penta-hepta defects within a perfect hexagonal pattern during directional solidification. However, we illustrate in Fig. 9 two of these penta-hepta defects that are sustained for the longest periods of time in our phase-field simulation. For the two defects (a) and (b), we show the time evolution of the number of neighbors of cells A and B forming the penta-hepta defect (top graph); the evolution of the normalized areas of cells A, B, and their neighboring cells C through J (bottom graph); as well as snapshots of the interface pattern on the right-hand side of Fig. 9. Within the penta-hepta defect in Fig. 9(a), which is maintained for 2 h, cells A (five neighbors) and B (seven neighbors) oscillate almost in phase opposition with each other. However, while some of the surrounding cells (gray symbols) seem to be in phase with cell A or B, they do not exhibit any clear breathing-mode oscillations. The continual topological evolution of the array induces for instance the phase shift between A and B in (a_2), in contrast to an almost perfect phase opposition in (a_1) and (a_3). Figure 9(b) also illustrates the behavior of a penta-hepta defect periodically switching to an hexagonal array as cells areas oscillate over a 1.5 h period of time. The two cells A and B also appear to be in phase opposition. When the areas of cells A and B are close to each other, the number of neighbors for the two cells may reach six as the pattern locally approaches a perfect hexagon, but when one of the two cells becomes much larger than the other, it becomes the cell with seven neighbors while the other only has five neighbors. Thus, in Fig. 9(b), cells A and B may switch from, respectively, seven and five neighbors in (b_2) to five and seven neighbors in (b_3). Later, as the amplitude of oscillations increases, cell A exhibits a tip-splitting event during the next oscillation period [not represented in Fig. 9(b)], hence further disturbing the local topological order.

An additional effect to consider is the curvature of the interface along the cylindrical cross section observed in our experiments [31], which may induce an overall movement

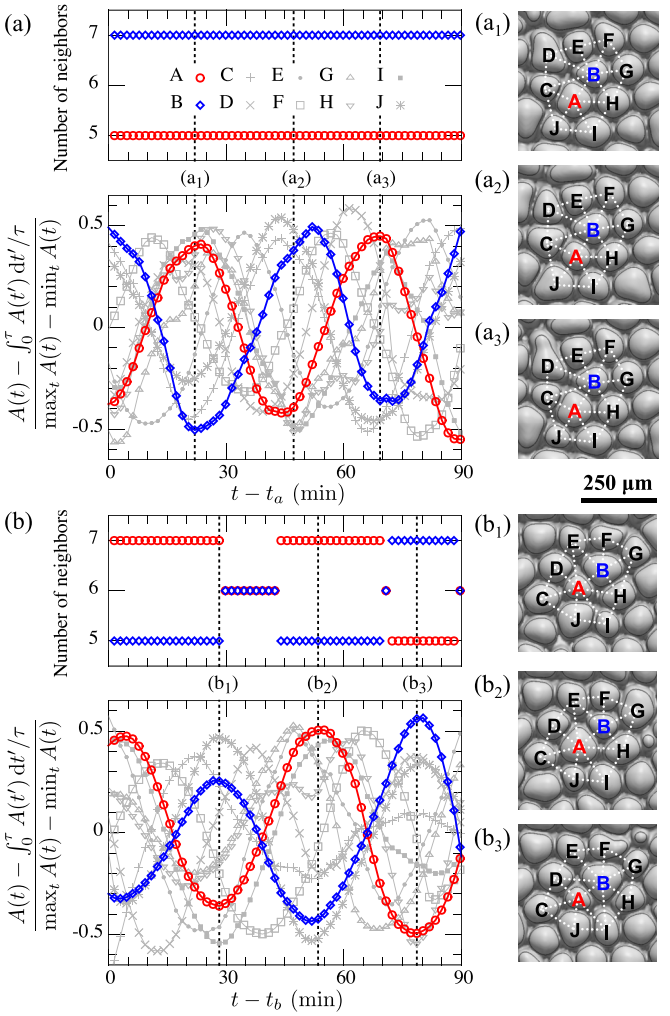

FIG. 9. (Color online) Oscillation dynamics of penta-hepta defects in the phase-field simulation of Fig. 7(b). For two different penta-hepta pairs of cells (A, B) in (a) and (b): The top panel shows the time evolution of the number of neighboring cells to cell A and cell B and the bottom graph shows the time evolution of the area of cells A (○), B (◇), as well as each surrounding cell C through J (gray symbols). Each cell area is normalized with respect to its time-averaged value $\int_0^\tau A(t')\,dt'/\tau$, its minimum, and its maximum value within the represented time range. Panels on the right-hand side illustrate the solid-liquid interface with labeled cells A through J at three different times respectively marked (a_k) and (b_k) on the left-hand side graphs. The time origin in (a) and (b) is, respectively, $t_a \approx 342$ min and $t_b \approx 162$ min.

of cells toward the center or the outside of the crucible, hence acting as a source of defects even in the absence of oscillations [55]. While the present article focuses on the origin and dynamics of breathing-mode oscillations, it would be interesting to investigate the dynamics of isolated penta-hepta defects within a perfect hexagonal pattern, which would not be limited to the narrow band of control parameters exhibiting oscillations.

In the remaining subsections, we use phase-field simulations to investigate the underlying mechanisms of the breathing-mode dynamics in 3D, more specifically focusing on hexagonal patterns, and we explore their dependence

upon growth conditions. To do so, we break down the problem into simpler subsystems of one (or, more accurately, a quarter of one) cell in Sec. IV B and of 1.5 cells with a forced hexagonal symmetry in Sec. IV C. These simulations help us explain the conditions for the occurrence of breathing modes, their link to the cell spacing stability range (Secs. IV B and IV D) and to the spatial order of the array (Sec. IV C), the long-time range dynamics of sustained breathing-mode oscillations (Sec. IV C), and, finally, the dependence of the oscillation period upon growth conditions (Sec. IV E).

B. Spatially in-phase oscillations of hexagonal patterns

As detailed in Sec. III D 2, we explore the range of individual cell stability imposing hexagonal boundary conditions on a quarter of cell in a domain of size $\Lambda/2 \times \Lambda\sqrt{3}/2$ in $x \times y$ for various Λ, G, and V.

First, for $\epsilon_4 = 0.007$ and $V = 1$ μm/s, we investigate the influence of the thermal gradient G. Figure 10(a) shows the resulting tip undercooling as a function of the cell spacing Λ (see Fig. 3) for all stable states identified between $G = 10$ and 28 K/cm. This graph shows a continuous branch of solutions at low $G \leqslant 12$ K/cm spanning until $\Lambda > 400$ μm. Increasing G, this continuous branch splits into two separate branches of solutions for $12 < G \leqslant 16$ K/cm. For $G = 18$ K/cm and above, only the leftmost (i.e., low spacing) branch remains. As expected, a lower temperature gradient broadens the stability range towards larger spacings.

Next, we investigated the influence of the solidification velocity on the stable spacing range, using $\epsilon_4 = 0.011$ and $G = 12$ K/cm, for velocities from $V = 0.5$ to 1.5 μm/s. The results, plotted in Fig. 10(b), display a similar pattern as in Fig. 10(a), with a continuous long branch of solutions for low undercooling, i.e., here for high velocities, and then a stable spacing gap at $V \leqslant 1.0$ μm/s, and, finally, the disappearance of the stable branch at high Λ for $V < 0.75$ μm/s. The presence of a spacing stability gap for low velocities is consistent with previous results from phase-field simulations on a model SCN-salol alloy [56].

An interesting result is the fact that toward the end of the leftmost stable branch, as well as at the limits of the rightmost branch for values of (G,V) exhibiting a stable spacing gap, cells at the limit of stability exhibit an oscillations of the tip position in time. This behavior usually occurs in a very narrow band of spacings, schematically illustrated with a thick gray line in Fig. 10. This spacing range typically lies between the last point represented in Fig. 10 and the next point (not drawn because unstable). The oscillation of cells at the end of a spacing stability branch was also already reported in phase-field simulations for a different alloy system [56] and could hence be a generic phenomenon in directional solidification.

Oscillations of the cell tip undercooling are illustrated in Fig. 11(a) for the three cells marked with black symbols at $G = 16$ K/cm in Fig. 10(a), i.e., for $\Lambda \approx 188$, 268, and 282 μm. At the end of the leftmost stable branch at $\Lambda \approx 188$ μm (○) as well as at the left end of the rightmost stable branch at $\Lambda \approx 282$ μm (□) the cell tip undercooling oscillates around its average value. In a very narrow range of spacings, these oscillations may be sustained for a few hours, e.g.,

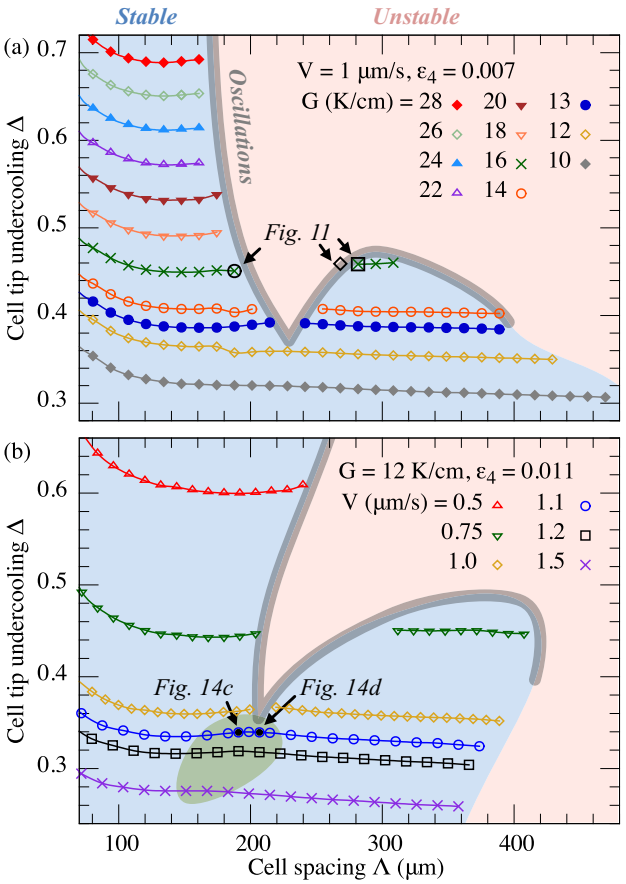

FIG. 10. (Color online) Phase-field predictions of stable states for hexagonal arrays of cells for different temperature gradients at a velocity $V = 1$ μm/s (a), and for different velocities at a temperature gradient $G = 12$ K/cm (b). The vertical axis Δ is the cell tip undercooling below the liquidus temperature normalized by the freezing range $mc_\infty(1 - 1/k)$. Calculations in (a) were performed with $\epsilon_4 = 0.007$, while calculations in (b) are with $\epsilon_4 = 0.011$. Both sets of parameters exhibit the opening of a stable spacing gap in the vicinity of $G = 12$ K/cm and $V = 1$ μm/s, yielding two stable branches when increasing G or decreasing V. The gray line in (a) and (b) illustrates schematically the limit of stability where cells exhibit oscillations of their position (i.e., undercooling) in time within a narrow range of spacings. This is exemplified for $V = 1$ μm/s and $G = 16$ K/cm at $\Lambda \approx 188$, 268, at 282 μm in Fig. 11. The green background zone for $V = 1.1$ to 1.5 μm/s in (b) illustrates the area investigated in Fig. 14, where breathing-mode oscillations can be induced by a change of growth conditions (see Sec. IV D), as exemplified at $V = 1.1$ μm/s in Figs. 14(c) and 14(d), respectively, for $\Lambda \approx 193$ and 206 μm.

for $\Lambda \approx 282$ μm (□). Most usually, they decay rapidly, but low-amplitude oscillations can be stimulated by adding noise, e.g., using $F_\psi = 0.03$ for $\Lambda \approx 188$ μm/s in Fig. 11(a) (○). Unstable spacings close to the limit of stability, such as $\Lambda \approx 268$ μm (◇), typically lead to oscillations increasing in amplitude and hence to a tip-splitting instability.

Our interpretation of the origin of these oscillations points at a complex interaction among the cell shape, the resulting amount of rejected solute in the liquid, the interface concentration, and the cell growth velocity. As illustrated in Fig. 11, oscillations of the cells vertical tip position, i.e., undercooling

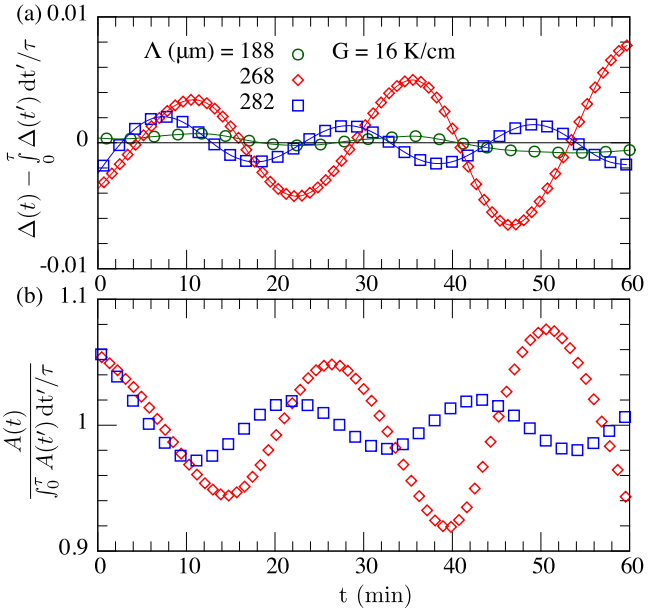

FIG. 11. (Color online) Phase-field prediction of the evolution of cell tip undercooling (a) and cell tip area (b) with time at $G = 16$ K/cm and $V = 1$ μm/s for stable cells at $\Lambda \approx 188$ (○) and 282 μm (□) and an unstable cell at $\Lambda \approx 268$ μm (◇), corresponding to the points marked with similar black symbols in Fig. 10(a).

[Fig. 11(a)], are correlated to their area [Fig. 11(b)], as a more advanced tip, i.e., a tip at lower undercooling, exhibits a larger area. Hence, at times when the cell tip is more advanced (i.e., the undercooling Δ is lower), the cell is larger, thereby rejecting more solute in the liquid and slowing down its growth. On the other hand, when the cell recoils in the temperature gradient frame (i.e., as Δ increases), the interface solute concentration increases, hence leading to an increase in solute gradient ahead of the interface, and a subsequent increase in growth velocity. The subtle interaction between interfacial equilibrium, solute-driven growth, and pattern evolution may thus give rise to oscillations in a narrow range of spacings for given control parameters. These oscillations involve similar interactions between the cell width and the diffusion boundary layer as the oscillations described by Karma and Pelcé [57]. However, the latter are specific to small spacings that are unstable to cell elimination. Oscillations over this small Λ range originate from the fact that the cell tip undercooling is a steeply decreasing function of spacing. In contrast, the oscillations discussed here occur at a much larger spacing, namely close to the high-Λ stability limit of the stable spacing range in presence of a spacing stability gap.

Such observations of individual cell oscillations tell us that a spatially in-phase oscillation of cells in 3D arrays is theoretically possible that stems from cells finding themselves at a spacing close to the limit between stability and instability. Hence, under given (G, V, Λ) conditions, each individual cell constitutes an oscillator. When combining several of these cells and oscillators together, microscopic fluctuations prevent all of them to beat in phase with each other, and they ultimately synchronize into a more stable configuration, namely a coupled $2\pi/3$ breathing-mode oscillation in the case of a hexagonal local order. Thus, in the following subsection, we show how combining three of these oscillating cells at the end of the left branch of solutions of Fig. 10 can result in a coherent breathing mode.

C. Spatially out-of-phase breathing oscillations of hexagonal patterns

For $V = 1$ μm/s, we investigate the synchronization of oscillating cells at the end of the left stable branch of Fig. 10(a). Figure 12 compares the breathing-mode evolution of cell areas in a local hexagonal array in experiments [Fig. 12(a)] to similar dynamics in a simulation at $G = 28$ K/cm and $\Lambda = 165$ μm [Fig. 12(b)], in a forced hexagonal array as described in Sec. III D.

As in experiments, the simulation in Fig. 12(b) exhibits a breathing mode of three subgroups of cells—labeled (A), (B, D, F), and (C, E, G)—oscillating nearly $2\pi/3$ out-of-phase with each other, with a period $\tau \approx 44.6$ min, which is close to the spatial average over the extended array both in simulations [$\tau \approx 48.1$ min in Fig. 7(b)] and experiments [$\tau \approx 45.6$ min

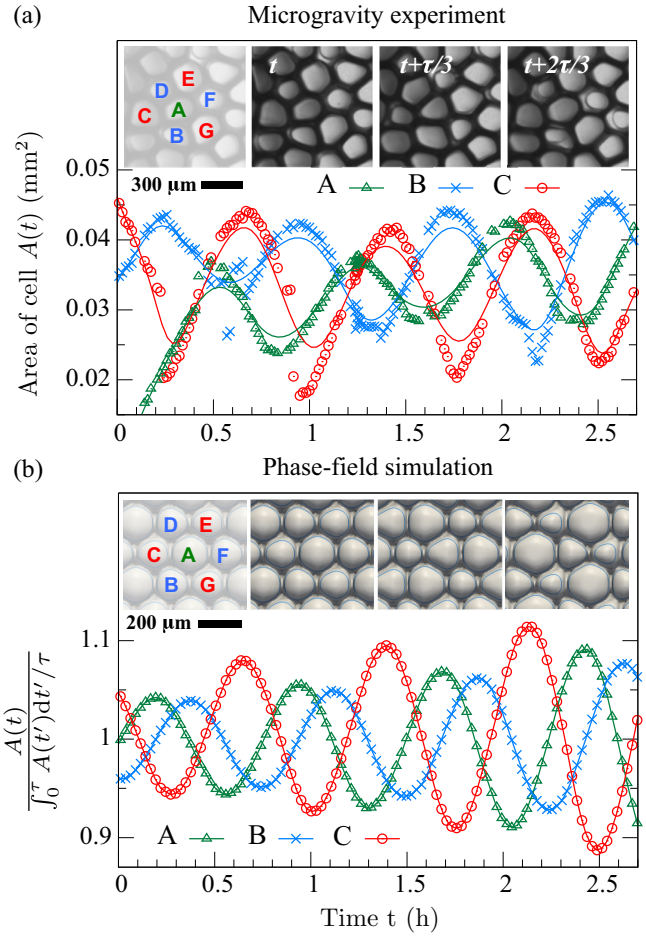

FIG. 12. (Color online) Short-range correlation of hexagonal patterns oscillations at $V = 1$ μm/s. Inside the "Hexagon" region of Fig. 7(a), three groups of cells oscillate coherently with a mutual phase difference of $\pm 2\pi/3$ (a). The phase-field simulation at $G = 28$ K/cm and $\Lambda = 165$ μm in (b) reproduces this coherent oscillation with a similar period.

in Fig. 7(a)]. For clarity we only plot the time evolution of the area of one cell of each group, i.e., cells A, B, and C in Fig. 12. However, the areas of other cells within the hexagon exhibit a time evolution similar to cell A, B, or C. While the oscillations in Fig. 12(b) are sustained at the scale of several hours, they exhibit an increase of the oscillation amplitude. This is consistent with experimental observations of several occurrences of breathing oscillations resulting in the tip splitting of one of the cells, subsequently at the origin of spatial rearrangement of the array. Similarly as in Fig. 11, the oscillations of the areas of cells are correlated with oscillations of their tip vertical position, i.e., undercooling (see, e.g., Fig. A3d in the Supplemental Material of Ref. [28] for an illustration of the oscillating hexagon of Fig. 12(b) seen from the side). It is worth mentioning that we could not find any $2\pi/3$ breathing-mode oscillatory regime starting from the oscillating cells at the end of the high-Λ stable spacing branches, as in these cases one cell usually gets quickly eliminated.

We found the longest sustained oscillations for a temperature gradient $G = 13$ K/cm at $\Lambda \approx 215$ μm, i.e., just at the opening of the stable spacing gap in Fig. 10(a). In order to reach this sustained state, we started from a hexagonal array at $G = 12$ K/cm with stable quarters of cell at $\Lambda \approx 215$ μm and increased G from 12 to 13 K/cm. Figure 13 shows that the resulting $2\pi/3$ breathing-mode oscillations observed at the scale of a few hours in Fig. 13(a) are sustained at the scale of more than 40 h in Fig. 13(b). Hence, while no stable state exists for a single cell at this spacing for these control parameters, the combination of three cells in a hexagonal breathing oscillation is stable at a long time scale.

Furthermore, at this time scale, the amplitude of the $A(t)$ oscillations in Fig. 13(b) displays an additional $2\pi/3$ breathing-mode oscillation, with a period of about 7 h. This oscillation period also appears clearly by plotting the difference of oscillation phase between each pair of cells (extracted following Sec. III E). Hence, in Fig. 13(c), we can see that the phase differences oscillate around the value $2\pi/3$, i.e., 120°. The time average of phases difference over 40 h in that specific case are between 118.8° and 121.0°. The presence of this second oscillation period explains why phase differences in large arrays are seldom exactly $2\pi/3$ [see, e.g., Fig. 8(b)], since even in a perfect hexagonal array all three phase differences at $2\pi/3$ never exactly occurs.

Additionally, with similar parameters (i.e., $G = 13$ K/cm and $\Lambda \approx 215$ μm), we performed a spatially extended simulation containing 24 cells by repeating 96 times the stable quarter of cell on the stable branch at $V = 1$ μm/s and $G = 12$ K/cm. That simulation resulted in an oscillation phase coherence over the entire array at the scale of more than 20 h. This result shows that long-range coherence is possible when starting from a perfect hexagonal arrangement and hence that the lack of long-range oscillation coherence is directly due to the absence of long-range spatial order of the array. Thus, long-range spatial coherence of oscillations observed so far in thin sample experiments in both cellular or eutectic arrays [13,21–25] may have been induced by forcing a quasi-2D spatial order in a confined array. In bulk three-dimensional experiments, such a long-range oscillation coherence seems very unlikely, due to both the intrinsic array dynamics [58] and the tip-splitting events that maintain the array disorder, unless externally forcing the spatial arrangement of the array, e.g., using local heating through laser or UV light [58–60].

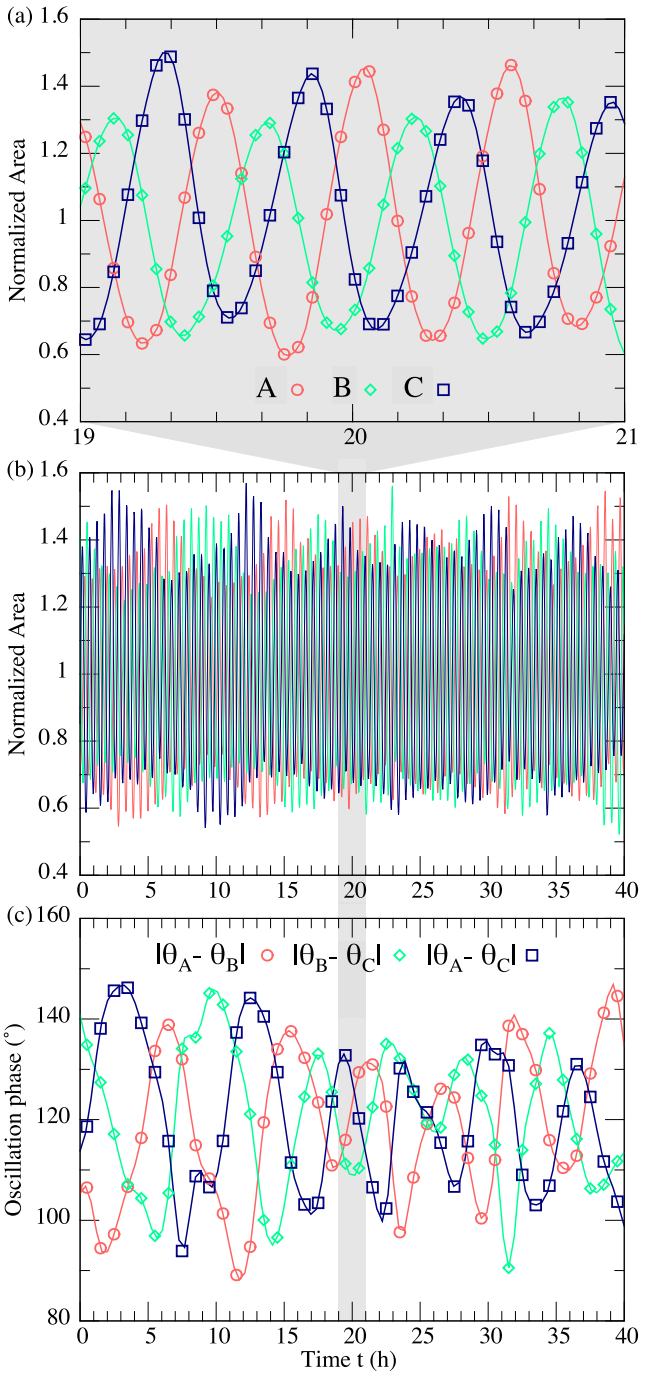

FIG. 13. (Color online) Sustained oscillations of cell areas for a hexagonal array at $G = 13$ K/cm, $V = 1$ μm/s, and $\Lambda \approx 215$ μm [see Fig. 10(a)]. The $2\pi/3$ breathing-mode oscillations appearing at the time scale of a few of hours in (a) are sustained in time, as shown over a 40 h time period in (b). This long-time scale dynamics exhibits an evolution of the oscillation amplitude of cell areas in (b), which also follows a $2\pi/3$ breathing mode with a period of approximately 7 h. This additional oscillation also appears in the evolution of phase difference between the three group of cells in (c), each oscillating around $2\pi/3$, i.e., 120°.

D. Relationship of spacing gap and oscillations

We have shown that a change of processing conditions can yield stable dynamical states that cannot be identified simulating a single cell (i.e., namely that a temperature gradient changing from 12 to 13 K/cm can yield a stable oscillatory state where a single cell is unstable at $\Lambda \approx 215$ μm). Following the same idea, it seems conceivable that a change of growth velocity may yield an oscillatory stable state for conditions in which a single cell is either unstable or stable but without oscillations.

We explored the possibility of observing breathing oscillations for control parameters yielding a continuous range of stable spacing, i.e., in a state where the individual cells do not exhibit oscillations. To do so, we used as initial conditions the final state of a simulation with 1.5 cells already in a $2\pi/3$ breathing-mode regime at $G = 12$ K/cm and $V = 1$ μm/s, corresponding to the last stable point of the leftmost branch in Fig. 10(b), i.e., for $\Lambda \approx 200$ μm. We used the resulting state as the initial state for simulations at $V = 1.1$, 1.2 μm/s, and beyond. For these velocities, we also explored different spacings by either stretching or shrinking the domain using bilinear interpolation of the fields to create initial conditions at larger or smaller spacing, respectively, similarly as for investigating stable branches for individual cells.

The results of those simulations, in Fig. 14, show that, depending on the history of the array, breathing modes can exist along continuous spacing branches. At $V = 1.1$ and 1.2 μm/s, open symbols in Fig. 14(a) denote simulations resulting in the elimination of one of the cells, thus ending with a π breathing-mode oscillation of two cells (to be investigated in further details and presented elsewhere). Full symbols represent simulations for which the $2\pi/3$ breathing mode of three cells was sustained for at least eight oscillation periods. At $V = 1.1$ μm/s, these breathing oscillations of cell areas are exemplified for $\Lambda = 193$ and 206 μm in Figs. 14(c) and 14(d). The normalized amplitude of the resulting $2\pi/3$ oscillations [Fig. 14(a)] decreases linearly with the array spacing from up to 0.8 (for $V = 1.1$ μm/s) to nearly zero. For larger spacings at $V \leqslant 1.2$ μm/s and for higher velocities $V > 1.2$ μm/s, the oscillation amplitude is very small, e.g., about 2% for $V = 1.3$ μm/s, and 0.5% for $V = 1.5$ μm/s. However, we think that these small oscillations remain relevant, as their oscillation period follows a similar trend as slower velocities (see Fig. 15 and corresponding discussion in the next subsection). Figure 14(b) shows a nonlinear dependence of the oscillation period with the spacing, with a limited absolute variation with Λ at a given V, i.e., a change of less than 20% over the entire spacing range. A similar decrease of oscillation period with spacing was already predicted by phase-field simulations of the 2λ-O mode in thin-sample experiments [61]. The dependence of the oscillation period with the growth velocity, which appears much more important than that with the spacing, is the focus of the following subsection.

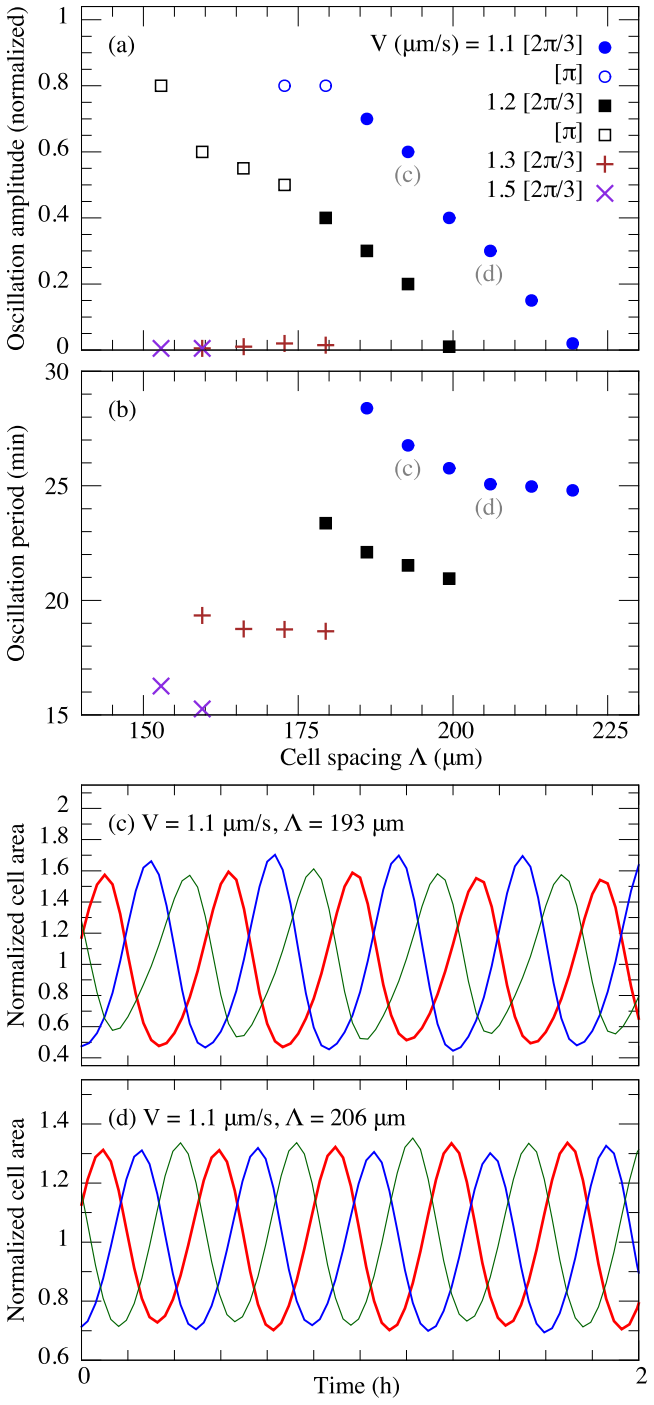

FIG. 14. (Color online) Presence of oscillatory breathing modes in continuous stable branches of spacing for $G = 12$ K/cm and $\epsilon_4 = 0.011$ [green background zone in Fig. 10(b)]. In (a), full symbols show the average normalized cell area oscillation amplitude for $2\pi/3$ breathing modes; open symbols represent simulations with elimination of one cell, resulting in π breathing oscillations of the two remaining cells. For $2\pi/3$ modes, the oscillation periods are given in (b). The area evolution with time for the three cells at $V = 1.1$ μm/s for $\Lambda = 193$ μm and $\Lambda = 206$ μm—tagged in (a), (b), and Fig. 10(b)—appear in (c) and (d), respectively.

E. Effects of growth conditions on oscillations

As illustrated by the similarity of the calculated oscillation periods at $G = 28$ K/cm in a spatially extended array [$\tau \approx 48.1$ min in Fig. 7(b)] and in an imposed hexagonal array [$\tau \approx 44.6$ min in Fig. 12(b)], the oscillation period seems unaffected by the spatial order of the array or lack thereof. Hence, its value

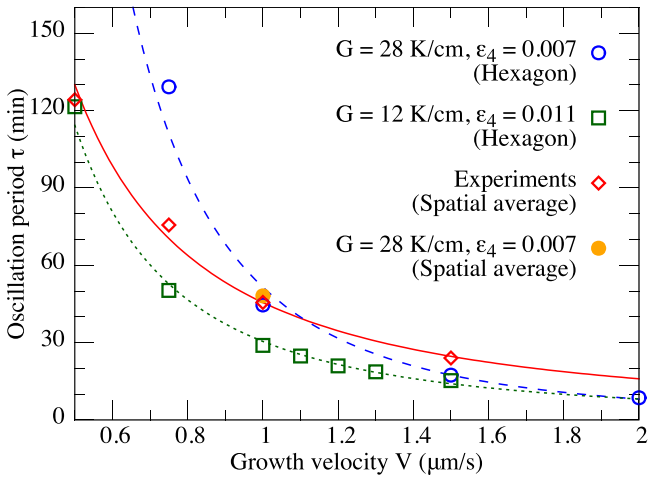

FIG. 15. (Color online) Oscillation period τ vs growth velocity V for ($\diamond$) experiments, ($\circ$) simulations with $\epsilon_4 = 0.007$ and $G = 28$ K/cm, and ($\square$) simulations with $\epsilon_4 = 0.011$ and $G = 12$ K/cm (see Sec. III C). Average oscillations periods from simulations of a spatially extended domain (full symbol at $V = 1$ μm/s) are similar to those for an imposed hexagonal pattern at the high spacing end of the leftmost stable spacing branch (open symbols). Data points are fitted to power laws $\tau \sim V^{\alpha}$ (lines). Simulations with $G = 28$ K/cm yield an exponent $\alpha \approx -2.67$. In contrast, simulations with a lower critical velocity $V_c \approx 0.26$ μm/s at $G = 12$ K/cm yield $\alpha \approx -1.91$, in better agreement with the experimental data with $\alpha \approx -1.51$.

depends only on experimental control parameters, namely the temperature gradient G and pulling velocity V.

We explore the dependence of τ with the growth velocity V for cellular arrays in a $2\pi/3$ out-of-phase breathing mode for the two limiting cases of $G = 28$ K/cm and $G = 12$ K/cm. To do so, we use the last (i.e., highest Λ) point on the left stable branch in Fig. 10 and repeat it in a hexagonal array of 1.5 cells, as explained in Sec. III D 3. For control parameters yielding a continuous stable spacing branch we also use the highest Λ where a $2\pi/3$ breathing mode occurs [see e.g., Fig. 14(b)]. These values of τ thus correspond to different values of Λ since the end of the stable branch occurs at different Λ for different G. However, as discussed in the previous subsection, for given (G, V) conditions the variation of τ with Λ remains limited [e.g., within 20% in Fig. 14(b)].

Figure 15 shows the cell oscillation period τ for velocities from 0.5 to 2 μm/s, in the experiments at $G \approx 19$ K/cm and in phase-field simulations with $\epsilon_4 = 0.007$ at $G = 28$ K/cm, and with $\epsilon_4 = 0.011$ at $G = 12$ K/cm. The values of $\tau(V)$ (symbols) are fitted to power laws $\tau \sim V^{\alpha}$ (lines). For the experiments, both the exponent and prefactor are similar to those found for breathing modes in confined thin-sample experiments [13], despite different alloys and geometries. While the similarity of the prefactor is likely coincidental, the power-law exponent of $-3/2$ may be generic to three-dimensional oscillations that stem from a spacing stability limit. (Note that in thin-sample experiments, while the spatial arrangement of cells is geometrically constrained to a quasi-2D configuration, the shape of the cells is three dimensional since the sample thickness is usually above 50 μm.)

At $V = 1$ μm/s the period predicted by phase-field simulations with $G = 28$ K/cm, which was the initial estimation of the experimental gradient, agrees very well with experiments, both from a spatial average over the spatially extended simulation in Fig. 7 ($\bullet$ in Fig. 15) and for an imposed hexagonal array at the end of the stable spacing branch from Fig. 10 ($\circ$). However, the power-law fit $\tau \sim V^{\alpha}$ for those simulations yields an exponent $\alpha \approx -2.67$, which differs from the experimental observations with $\alpha \approx -1.51$. Our interpretation is that the discrepancy is due to an overestimation of the critical velocity for the onset of morphological instability $V_c = DGk/[(k-1)mc_{\infty}] \approx 0.61$ μm/s when using $G = 28$ K/cm and $k = 0.21$, when cellular patterns are already present at $V = 0.5$ μm/s in the experiment.

As $V \to V_c$ we expect τ to deviate from the scaling regime described by a $-3/2$ exponent, which hence only can be found for velocities that are significantly larger than V_c. For a lower $V_c \approx 0.26$ μm/s with $G = 12$ K/cm, the power-law exponent $\alpha \approx -1.91$ in Fig. 15 is in much better agreement with experiments. As pointed out in Sec. III C, a recent study [31] of the transient recoil of the planar interface has led us to consider a temperature gradient $G = 19$ K/cm, together with a likely influence of the thermal history of the setup on the final selected structures and dynamics. This study also suggested that in this composition range, the solute partition coefficient could be lower than the value found in the literature (namely $k \approx 0.138$ instead of 0.21), which could explain the lower value of V_c without considering a gradient as low as $G = 12$ K/cm. These aspects warrants further investigations, which are currently underway.

V. SUMMARY AND CONCLUSIONS

We have proposed an in-depth phase-field study of breathing-mode oscillations identified in three-dimensional cellular arrays during solidification in reduced gravity. Our simulations reproduce the salient features observed in experiments, namely:

(i) within a narrow range of control parameters, every cell in the solidification front exhibits oscillations of its cross-section area and tip height;

(ii) this range of control parameters includes primarily cases where a spacing gap exists in the branch of steady-state growth solutions;

(iii) simulations in this range of parameters yield oscillations of a single cell, equivalent to an in-phase oscillation of an entire array with perfect hexagonal symmetry;

(iv) when combining such cells in a larger hexagonal array simulation (i.e., with three halves of cells or more), small fluctuations destroy the in-phase synchronization of cells in the array, thereby leading to a $2\pi/3$ out-of-phase oscillatory breathing mode of three groups of cells;

(v) in both experiments and simulations, spatially extended cellular arrays exhibit spatial disorder, which is maintained by frequent tip-splitting events promoted by oscillations that grow in amplitude;

(vi) the oscillation period of cells is remarkably homogeneous throughout spatially extended arrays;

(vii) while the oscillations in spatially extended arrays do not exhibit long-range coherence, local hexagonal order yields

$2\pi/3$ out-of-phase breathing modes, and penta-hepta defects can lead to localized π out-of-phase breathing modes (i.e., phase opposition).

These observations are in sharp contrast with previous reported simulations and experiments on breathing modes during solidification of confined structures in thin samples that exhibited long-range coherent oscillations [13,21–25]. They also differ in that tip-splitting instabilities in thin-sample experiments usually lead to stable multiplet structures [13], while in our case they only disturb the array spatial order.

Our simulations have shown that the oscillatory behavior of cells is linked to the stable spacing range of a cellular array. At low dimensionless tip undercooling Δ (i.e., high velocity and/or low temperature gradient), the stable cell spacing Λ spans a broad continuous range (Fig. 10). At intermediate Δ, the stable spacing range exhibits two separate branches with a gap between them that increases with Δ, as suggested by earlier phase-field calculations [56]. At high Δ the stable branch for higher Λ disappears and only one branch remains. In the presence of a Λ stability gap, or at higher Δ (i.e., lower V or higher G), individual cells exhibit oscillations at the ends of stable spacing branches.

The combination of several cells in this oscillatory state at the end of the low-Λ branch leads to the short-range synchronization of cells and hence to breathing-mode oscillations. Thus, depending upon the local spatial organization, cells will locally start beating in phase opposition (in presence of a square pattern) or with a $2\pi/3$ phase shift with one another (in presence of a hexagonal pattern). The most spatiotemporally stable breathing-mode oscillations occur just at the opening of the stable spacing gap, i.e., here for $V \approx 1$ μm/s and $G \approx 13$ K/cm. In hexagonal arrays, in addition to the $2\pi/3$ breathing mode of cells areas with a period of about 45 min for $V = 1$ μm/s, sustained oscillations exhibit a second $2\pi/3$ breathing oscillation of the cell area oscillations amplitude and of the phase shift between cells. Thus, the phase shift between the three groups of cells oscillates around $2\pi/3$ with a period of several hours (e.g., here approximately 7 h for $V = 1$ μm/s in Fig. 13).

For other parameters in the vicinity of the stable spacing gap, oscillations are still possible that are sustained at the time scale of several hours. However, most of them display a progressive decrease or increase of the oscillation amplitude, the latter leading to the tip splitting of one cell, as observed in experiments. Moreover, a change in growth velocity V or thermal gradient G can lead to oscillatory breathing modes for conditions at which an individual cell would be either unstable (e.g., Fig. 13) or stable without oscillations (e.g., Fig. 14). Further away from these parameters (e.g., at lower G and/or higher V), we did not observe oscillatory modes. This may explain why in experiments performed at lower G, tip-splitting instabilities lead to stable multiplet structures rather than oscillations, since the stable spacing range in these conditions is likely very wide and includes a variety of stable asymmetric cells.

We found that a perfectly hexagonal array of cells yields a long-range spatiotemporal coherence of breathing oscillations. This confirms that the lack of global coherence in the experiments is due to the spatial disorder of the array. This disorder originates in both experiments and simulations from the amplification of noise by morphological instability during the transient recoil of the interface. It is then maintained by the spatiotemporal dynamics of the array, as oscillations contribute to maintaining this disorder. These results suggest that the long-range coherent oscillations reported so far in thin-sample experiments and 2D simulations are induced by the imposed spatial order resulting from confinement. Hence, while tip-splitting instabilities tend to stabilize thin-sample oscillatory structures into multiplets, in 3D tip splitting only contributes to the disorder of the oscillatory array and subsequently to the lack of long-range oscillations coherence. These observations then make it very unlikely to observe long-range correlated oscillations in spatially extended cellular arrays, unless possibly by forcing their spatial organization [59,60,62].

Finally, while the dependence of the oscillation period τ upon G is limited, its dependence upon V is quantitatively significant (Fig. 15). The experiments exhibit a power-law scaling $\tau \sim V^{\alpha}$ with an exponent $\alpha = -3/2$, similar to that observed in thin-sample experiments [13]. Phase-field simulations have shown that, while $\tau(V)$ deviates from a power law as V gets close to the critical velocity V_c, when V is large enough compared to V_c the predicted power-law exponent α becomes close to $-3/2$. These results suggest that the $\tau \sim V^{-3/2}$ scaling law may be generic to oscillatory modes stemming from a spacing stability limit.

Beyond the oscillatory states investigated in the present work, the wealth of experimental data made available by those unique three-dimensional microgravity directional solidification experiments opens several new avenues of investigations. One important area of investigation is the dynamical selection of the cellular or dendritic array spacing. In particular, the origin of the discrepancy between the selected spacings observed in experiments and phase-field simulations, which may be due to the influence of the thermal history [31] on spacing selection, warrants further study. A related problem is the dynamical selection of the array structure. While cells tend to organize predominantly in hexagonal arrays, this ordering is suppressed by the formation of well-developed secondary branches. Which structure is favored as a function of growth conditions is still not well understood, in particular in the vicinity of the cell-to-dendrite transition. Moreover, while it is well recognized that the selection of both the array spacing and structure can be further influenced by crystal orientation, as well as grain boundaries in the presence of several grains [38,63], those effects remain largely unexplored in spatially extended three-dimensional samples. Work to address several of those issues by detailed quantitative analyses of microgravity experimental data and phase-field simulations is currently underway.

ACKNOWLEDGMENTS

This research was achieved thanks to the support of NASA through Grants No. NNX07AK69G and No. NNX14AB34G, CNES through the MISOL3D project (MIcrostructures de SOLidification 3D), and Région PACA through the ENEMS project (Étude Numérique et Expérimentale des Microstructures de Solidification).

[1] R. Wlodawer, *Directional Solidification of Steel Castings* (Pergamon Press, London, 1966).
[2] W. Kurz and D. J. Fisher, *Fundamentals of Solidification*, 3rd ed. (Trans Tech, Zurich, 1992).
[3] J. Campbell, *Castings* (Butterworth-Heinemann, London, 2003).
[4] D. M. Stefanescu, *Science and Engineering of Casting Solidification*, 2nd ed. (Springer, Berlin, 2008).
[5] J. S. Langer, Lectures on the Theory of Pattern Formation, in *Chance and Matter (Les Houches, Session XLVI)*, edited by J. Souletie, J. Vannimenus, and R. Stora (North-Holland, Amsterdam, 1987).
[6] M. C. Cross and H. Greenside, *Pattern Formation and Dynamics in Nonequilibrium Systems* (Cambridge University Press, Cambridge, 2009)
[7] W. W. Mullins and R. F. Sekerka, J. Appl. Phys. **35**, 444 (1964).
[8] M. E. Glicksman, Mater. Sci. Eng. **65**, 45 (1984).
[9] R. Trivedi and K. Somboonsuk, Acta Metallurg. **33**, 1061 (1985).
[10] H. Esaka, W. Kurz, and R. Trivedi, Evolution of primary dendrite spacing in succinonitrile-acetone alloys, in *Solidification Processing*, edited by J. Beech and H. Jones (The Institute of Metals, London, 1988).
[11] B. Billia and R. Trivedi, in *Handbook of Crystal Growth*, edited by D. T. J. Hurle (North-Holland, Amsterdam, 1993).
[12] R. Trivedi and W. Kurz, Int. Mater. Rev. **39**, 49 (1994).
[13] M. Georgelin and A. Pocheau, Phys. Rev. Lett. **79**, 2698 (1997).
[14] M. Georgelin and A. Pocheau, Phys. Rev. E **57**, 3189 (1998).
[15] W. Losert, B. Q. Shi, and H. Z. Cummins, Proc. Natl. Acad. Sci. U.S.A. **95**, 431 (1998).
[16] W. Losert, B. Q. Shi, and H. Z. Cummins, Proc. Natl. Acad. Sci. U.S.A. **95**, 439 (1998).
[17] A. Pocheau and M. Georgelin, J. Cryst. Growth **206**, 215 (1999).
[18] H. Jamgotchian, N. Bergeon, D. Benielli, P. Voge, B. Billia, and R. Guérin, Phys. Rev. Lett. **87**, 166105 (2001).
[19] K. Nagashimaa and Y. Furukawa, J. Cryst. Growth **237-239**, 81 (2002).
[20] C. Misbah and A. Valance, Phys. Rev. E **49**, 166 (1994).
[21] P. E. Cladis, J. T. Gleeson, P. L. Finn, and H. R. Brand, Phys. Rev. Lett. **67**, 3239 (1991).
[22] B. Grossmann, K. R. Elder, M. Grant, and J. M. Kosterlitz, Phys. Rev. Lett. **71**, 3323 (1993).
[23] P. Kopczynski, W.-J. Rappel, and A. Karma, Phys. Rev. Lett. **77**, 3387 (1996).
[24] A. Karma and A. Sarkissian, Metallurg. Mater. Trans. A **27**, 635 (1996).
[25] M. Ginibre, S. Akamatsu, and G. Faivre, Phys. Rev. E **56**, 780 (1997).
[26] K. Kassner, J.-M. Debierre, B. Billia, N. Noël, and H. Jamgotchian, Phys. Rev. E **57**, 2849 (1998).
[27] M. Plapp and M. Dejmek, Europhys. Lett. **65**, 276 (2004).
[28] N. Bergeon, D. Tourret, L. Chen, J.-M. Debierre, R. Guérin, A. Ramirez, B. Billia, A. Karma, and R. Trivedi, Phys. Rev. Lett. **110**, 226102 (2013).
[29] N. Bergeon, C. Weiss, N. Mangelinck-Noël, and B. Billia, Trans. Ind. Inst. Metallurg. **62**, 455 (2009).
[30] N. Bergeon, A. Ramirez, L. Chen, B. Billia, J. Gu, and R. Trivedi, J. Mater. Sci. **46**, 6191 (2011).
[31] F. L. Mota, N. Bergeon, D. Tourret, A. Karma, R. Trivedi, and B. Billia, Acta Mater. **85**, 362 (2015).
[32] See Supplemental Material at http://link.aps.org/supplemental/10.1103/PhysRevE.92.042401 for videos corresponding to Figures 1(a), 4(a), and 4(d).
[33] B. Echebarria, R. Folch, A. Karma, and M. Plapp, Phys. Rev. E **70**, 061604 (2004).
[34] B. Echebarria, A. Karma, and S. Gurevich, Phys. Rev. E **81**, 021608 (2010).
[35] K. Glasner, J. Comput. Phys. **174**, 695 (2001).
[36] A. Karma and W.-J. Rappel, Phys. Rev. E **53**, R3017 (1996).
[37] A. Karma and W.-J. Rappel, Phys. Rev. E **57**, 4323 (1998).
[38] D. Tourret and A. Karma, Acta Mater. **82**, 64 (2015).
[39] CUDA.: *Compute Unified Device Architecture Programming Guide* (Nvidia, Santa Clara, CA, 2007).
[40] A. Karma and W.-J. Rappel, Phys. Rev. E. **60**, 3614 (1999).
[41] J. Ghmadh, J.-M. Debierre, J. Deschamps, M. Georgelin, R. Guérin, and A. Pocheau, Acta Mater **74**, 255 (2014).
[42] J. Teng and S. Liu, J. Cryst. Growth **290**, 248 (2006).
[43] S. Liu, J. Teng, and J. Choi, Metallurg. Mater. Trans. A **38**, 1555 (2007).
[44] R. Trivedi (unpublished).
[45] M. Xu, L. M. Fabietti, Y. Song, D. Tourret, A. Karma, and R. Trivedi, Scripta Mater. **88**, 29 (2014).
[46] N. Bergeon *et al.* (unpublished).
[47] L. S. Tsimring, Phys. Rev. Lett. **74**, 4201 (1995).
[48] L. S. Tsimring, Physica D **89**, 368 (1996).
[49] M. C. Cross and P. C. Hohenberg, Rev. Mod. Phys. **65**, 851 (1993).
[50] S. Ciliberto, P. Coullet, J. Lega, E. Pampaloni, and C. Perez-Garcia, Phys. Rev. Lett. **65**, 2370 (1990).
[51] P. Cerisier, C. Perez-Garcia, C. Jamond, and J. Pantaloni, Phys. Rev. A **35**, 1949 (1987).
[52] A. M. Turing, Phil. Trans. R. Soc. Lond. B **237**, 37 (1952).
[53] T. Tam, D. Ohata, and M. Wu, Phys. Rev. E **61**, R9 (2000).
[54] W. J. Firth, SPIE Proc. **2039**, 290 (1993).
[55] N. Bergeon, F. L. Mota, L. Chen, D. Tourret, J.-M. Debierre, R. Guérin, A. Karma, and B. Billia, and R. Trivedi, IOP Conf. Ser.: Mater. Sci. Eng. **84**, 012077 (2015).
[56] S. Gurevich, A. Karma, M. Plapp, and R. Trivedi, Phys. Rev. E **81**, 011603 (2010).
[57] A. Karma and P. Pelcé, Phys. Rev. A **39**, 4162 (1989).
[58] P. Cerisier, S. Rahal, and B. Billia, Phys. Rev. E **54**, 3508 (1996).
[59] K. Lee and W. Losert, J. Cryst. Growth **269**, 592 (2004).
[60] S. Akamatsu, K. Lee, and W. Losert, J. Cryst. Growth **289**, 331 (2006).
[61] J. Ghmadh, Etude par la méthode du champ de phase à trois dimensions de la solidification dirigée dans des lames minces, Ph.D. Thesis, Aix-Marseille Université, 2014.
[62] A. J. Pons, A. Karma, S. Akamatsu, M. Newey, A. Pomerance, H. Singer, and W. Losert, Phys. Rev. E **75**, 021602 (2007).
[63] Ch.-A. Gandin, M. Eshelmann, and R. Trivedi, Metallurg. Mater. Trans. A **27A**, 2727 (1996).